Micromechanical modelling of deformation and fracture of hydrating cement paste using X-ray computed tomography characterisation

CrossMark

Mingzhong Zhang [a, b, *], Andrey P. Jivkov [b]

[a] *Advanced and Innovative Materials (AIM) Group, Department of Civil, Environmental and Geomatic Engineering, University College London, London WC1E 6BT, UK*
[b] *School of Mechanical, Aerospace and Civil Engineering, The University of Manchester, Manchester M13 9PL, UK*

A B S T R A C T

Cement paste is the basic but most complex component in cement composites, which are the dominant construction material in the world. Understanding and predicting elastic properties and fracture of hydrating cement paste are challenging tasks due to its complex microstructure, but important for durability assessments and life extension decisions. A recently proposed microstructure-informed site-bond model with elastic-brittle spring bundles is developed further to predict the evolution of elastic properties and fracture behaviour of cement paste. It is based on microstructural characteristics of hydrating cement paste obtained from X-ray computed microtomography (micro-CT) with a spatial resolution of 0.5 µm/voxel. Volume fraction and size distribution of anhydrous cement grains are used to determine the model length scale and pore-less elasticity. Porosity and pore size distribution are used for tuning elastic and failure properties of individual bonds. The fracture process is simulated by consecutive removal of bonds subjected to surface energy based failure criterion. The stress–strain response and elastic properties of hardened cement pastes with curing ages of 1, 7 and 28 days are obtained. The simulated Young's modulus and deformation response prior to peak stress agree very well with the experimental data. The proposed model provides an effective tool to evaluate time evolution of elastic properties and to simulate the initiation, propagation, coalescence and localisation of micro-cracks.

1. Introduction

Cement composites are the most popular and widely used construction material in the world. The understanding and prediction of elastic properties and fracture behaviour of such material are of significant technological importance and scientific interest, as they play a crucial role in the durability assessments and life extension decisions of reinforced concrete structures. The time evolution of elastic properties and fracture of such material are complicated since they strongly depend on its heterogeneous and multiphase microstructure, which generally ranges over several length scales from nanometres to metres and develops over time as a result of continued hydration of the cement [1]. At meso-scale, concrete can be considered as a three-phase composite consisting of aggregate, bulk cement matrix and interfacial transition zone (ITZ) between them. ITZ is actually a "special" cement paste with higher porosity and larger pores relative to the bulk cement matrix [1,2]. Therefore, as the most complicated and basic component in cement-based materials, the mechanical properties and fracture of cement paste accounting for microstructure should be studied in detail firstly.

Because of its significance, a lot of efforts, both experimentally and numerically, have been made to study the evolution of elastic properties and cracks of hydrating cement paste in the past decades. Among them, micromechanical modelling approaches show a great advantage because some main microstructure information can be taken into account. These approaches can be classified into three general categories: analytical models, continuum-based numerical models and discrete lattice models.

With respect to analytical models, Bernard et al. [3] proposed a multistep micromechanics homogenization approach based on effective medium approximation scheme in combination with a kinetics model of the four main hydration reactions of ordinary Portland cement to predict the time evolution of elastic properties

* Corresponding author. Advanced and Innovative Materials (AIM) Group, Department of Civil, Environmental and Geomatic Engineering, University College London, London WC1E 6BT, UK. Tel.: +44 20 7679 7299.
E-mail address: mingzhong.zhang@ucl.ac.uk (M. Zhang).

of cement paste. Cement paste is regarded as a composite of calcium-silicate-hydrate (C—S—H) matrix with large calcium hydroxide (CH) crystals, cement clinker inclusions and pores, which have different mechanical properties. Based on the same procedure, Constantinides and Ulm [4] estimated the effect of two types of C—S—H, i.e., high-density C—S—H and low-density C—S—H, on the macroscopic elastic properties of hydrating cement paste with water-to-cement (w/c) ratio of 0.5 in a quantitative manner. Sanahuja et al. [5] developed a similar homogenization scheme to estimate the evolution of effective elastic moduli of hydrating cement paste that is modelled as a four-phase material made up of anhydrous cement grains, inner hydration products surrounding the anhydrous particles, outer hydration products and pores. The simulated Young's moduli of cement paste during hydration were in excellent agreement with the experimental results available in the literature. Zheng et al. [6] and Zhao and Chen [7] predicted the elastic moduli of hardened cement paste at various curing ages with various w/c ratios by using a simple three-step analytical homogenization scheme. In this scheme, hardened cement paste is modelled as n-layer composite including spherical unhydrated cement particles, C—S—H, CH and capillary pores. Pichler and Hellmich [8], and Pichler et al. [9] modelled cement paste as a two-phase composite material composed of hydrate foam and spherical cement inclusions, and used the Mori-Tanaka (M-T) [10] scheme to determine the effective elastic moduli of cement paste, which are considered as input to further investigate the mechanical properties of mortar. Although analytical models are able to provide simple expressions for estimation of elastic properties of cement paste, the proposed simplified multiphase or n-layer cement hydration models need further validation prior to applications of them.

Regarding continuum-based numerical models, finite element method (FEM) is the most widely used one. Haecker et al. [11] utilised a computer-based cement hydration model, CEMHYD3D [12], to generate the 3D digital microstructure of cement paste consisting of unhydrated cement, hydration products and pore space, and then quantitatively predicted the elastic moduli of cement paste as a function of degree of hydration by using three-dimensional (3D) FEM. The required individual phase moduli were obtained from literature. Smilauer and Bittnar [13] predicted the elastic properties of hydrating cement paste by combining the CEMHYD3D model, percolation theory and finite element analysis. The size of the representative volume element (RVE) of cement paste was found to be $50 \times 50 \times 50$ μm. Similarly, a combination of CEMHYD3D model and FEM was applied to estimate the evolution of effective elastic modulus and diffusion coefficient of cement paste with w/c ratio of 0.4 during hydration [14–16]. Hain and Wriggers [17] obtained the 3D microstructure of hardened cement paste from X-ray computed microtomography (micro-CT) with a spatial resolution of 1.0 μm/voxel and carried out microstructure-based modelling of effective elastic properties of cement paste via homogenization. A series of numerical-statistical analyses were performed to determine the RVE size for measuring elasticity of cement paste. Recently, Huang et al. [18] proposed a statistical numerical homogenization procedure through FEM to study the effective elastic properties of cement paste based on X-ray micro-CT images with a resolution of 0.95 μm/voxel. The mean values of the simulated elastic properties were in good agreement with the experimental data. Although the continuum approach is capable of predicting the mechanical properties of cement paste based on microstructure, it is inherently incapable of dealing with fracture process in cement paste, e.g., crack initiation, propagation and coalescence. In addition, the spatial resolution of X-ray CT was limited to 1.0 μm that is not high enough to obtain a realistic

microstructure of cement paste. Therefore, X-ray CT with a higher resolution is required.

In regard to discrete lattice models, they offer a promising modelling strategy to investigate the mechanical properties and explain fracture processes in cement paste because of its unique feature of representing a material by a lattice system of beam or spring elements [19]. Qian et al. [20] further developed and applied the lattice beam model proposed by Schlangen and van Mier [21] based on the simplest regular lattice with cubic cells to predict the mechanical properties and fracture of hydrating cement paste. The used 3D microstructures of cement pastes at different curing ages were simulated by using a cement hydration model, HYMOSTRUC3D [22–25]. However, the simulated stress—strain response of cement paste under uniaxial tension seems too brittle and remains not realistic [26]. Additionally, this lattice model is not physically realistic in terms of shape of the represented phases in cement paste and unable to provide a linear elastic response with an appropriate elastic modulus and Poisson's ratio [27]. To overcome such limitations, Jivkov and Yates [27] proposed a novel bi-regular lattice beam model based on truncated octahedral cells, namely, site-bond model, to study the elasticity of solids and further successfully utilized to predict the mechanical behaviour, and micro-crack population and damage evolution in cement-based materials considering microstructural characteristics [19,28]. Nevertheless, this model has a shortcoming that the relationship between the global elasticity and properties of local beam elements cannot be analytically derived [29]. In order to improve this aspect, Zhang and Jivkov [29] reformulated the site-bond model by replacing beam elements with spring elements and predicted the damage evolution in hardened cement paste.

The main purpose of this work is to further develop the proposed site-bond model and apply it to simulate the elastic properties and fracture behaviour of hydrating cement paste taking into account its microstructural information. The microstructural characteristics, such as pore size distribution, porosity, and volume fraction and size distribution of anhydrous cement grains are derived from high-resolution X-ray micro-CT images along with a series of image processing and analyses. The 3D microstructure of cement paste comprised of anhydrous cement grains, hydration products and pores is represented by an assembly of truncated octahedral cells with sites at cell centres and bonds linking the neighbouring cells. The simulated site-bond assembly is then subjected to uniaxial tensile loading and stress—strain response of cement paste is obtained. The fracture process is simulated by the removal of failed bonds. The simulation results are compared with the available experimental data.

2. Microstructural characterisation of cement paste using X-ray micro-CT

2.1. X-ray micro-CT imaging

The 3D microstructure of hardened cement paste used in this work was obtained from X-ray micro-CT scans. ASTM type I Portland cement was used. The w/c ratio of the cement paste specimen was 0.5 (mass ratio). After drill mixing in a plastic beaker, small parts of the paste were poured into the syringe and then injected into a micro plastic tube with an internal diameter of 250 μm. The specimen was stored in the standard curing room with a relative humidity of 95% and temperature of 20 °C and scanned at 1, 7 and 28 days. A high resolution Xradia MicroXCT-200 CT scanner at the Beckman Institute for Advanced Science and Technology at the University of Illinois at Urbana—Champaign was used for acquiring projection images with a source power of 10 W at 50 kV. The sample was rotated on the stage from −91° to 91° at an increase of

0.25° generating 729 shadow projections with a pixel size of 0.5 μm. To the best of the authors' knowledge, this resolution is by far the highest one reported for 3D non-destructive imaging of cement-based materials. Each projection image was averaged from frames within an exposure time of 12 s. The image reconstruction was performed using the algebraic method implemented in the Xradia reconstruction software that results in a 3D stack of virtual 8-bit cross-section images with grayscale values from 0 to 255. The reader is referred to [30] for further information on the X-ray micro-CT testing.

A cylindrical region of interest (ROI) with 200 μm in diameter and 100 μm (200 slices) in thickness was extracted from the centre of the reconstructed 3D images where the cement paste is considered to be the most homogeneous. Fig. 1 shows the micro-CT grey images of ROI of cement paste with curing ages of 1, 7 and 28 days, respectively. The dark phase stands for capillary pores. The white phase corresponds to anhydrous cement grains (unhydrated cement particles). The grey phases most probably represent hydration products. The hydration of cement proceeds with increasing curing age, as a result of which cement (i.e. white phase) and water (i.e. dark phase) are continuously consumed and an increasing number of hydration products (i.e. grey phase) appear in cement paste. In order to identify these three phases in cement phase and quantify their content, a series of image processing and analysis are required, which are described in detail in the following section.

2.2. Microstructural characterisation

As discussed in Ref. [30], many approaches have been proposed and developed for image segmentation. Here the global thresholding method is applied and implemented by using ImageJ, a public domain Java-based image processing program (National Institutes of Health, USA). Based on the grey-level histogram two threshold grey values are defined to segment pores from anhydrous cement grains and hydration products, and subsequently segment anhydrous cement grains from hydration products. Fig. 2 illustrates the identified capillary pores and anhydrous cement grains in cement paste at curing age of 7 days, which is shown in Fig. 1b. As a result, the original grey scale image is converted into a ternary image consisting of pore, anhydrous cement grain and hydration product. With this ternary image, the microstructural characteristics, such as porosity, grain density of anhydrous cement, size distributions of pore and anhydrous cement grain of ROI can be gained in a quantitative manner after a series of image analysis. More details about the image processing and analysis can be found in a previous work [29] and [31].

The porosity and volume fraction of anhydrous cement grains of cement paste at 1, 7 and 28 days are found to be 25.69% and 22.34%, 18.71% and 15.67%, and 12.58% and 8.65%, respectively. Besides pore and anhydrous cement, the other volume is occupied by hydration products. It should be mentioned that the individual phase with size less than 0.5 μm cannot be identified separately due to the limited spatial resolution. As curing age increases, both porosity and volume fraction of anhydrous cement grain of cement paste decreases, while the volume fraction of hydration product increases. Fig. 3 shows the obtained porosity for each 2D image of cement paste along Z-direction from top to bottom (200 slices, 100 μm). It indicates that 28-day old cement paste has less fluctuation in porosity along the thickness of sample compared to cement paste at 1 and 7 days.

Assuming spherical shapes for pore and particle, the experimental size (i.e. equivalent radius) distributions of pore and unhydrated cement particle are determined by summarising the volume of each separate cluster in ternary image of cement paste. Fig. 4 shows the obtained pore and unhydrated cement particle size
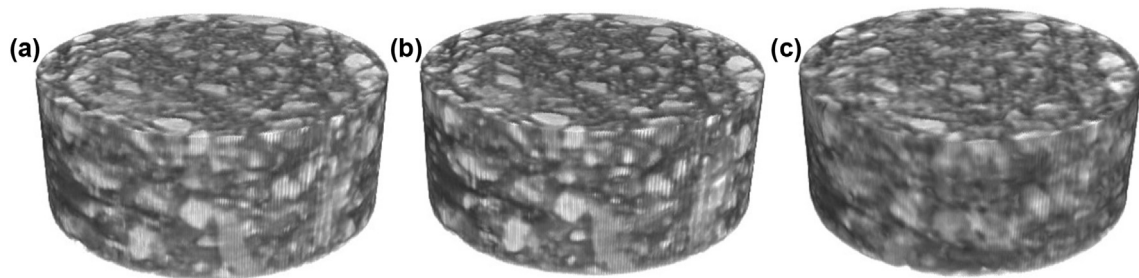

Fig. 1. Micro-CT images of hydrating cement pastes with 200 μm in diameter and 100 μm with curing ages of (a) 1 day; (b) 7 days; (c) 28 days. The dark, white and grey phases represent capillary pore, anhydrous cement grain and hydration product, respectively.
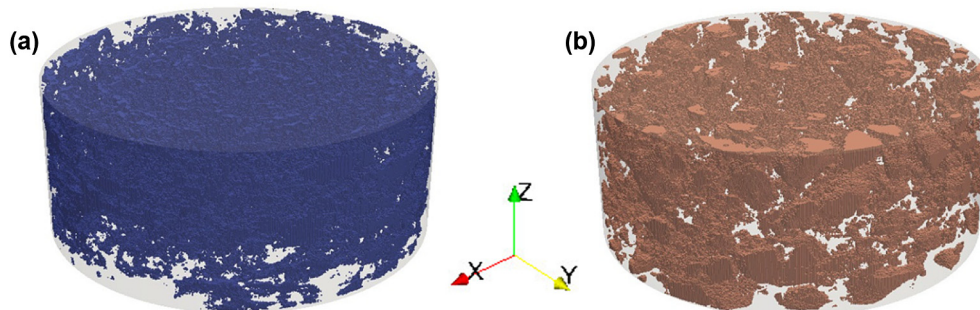

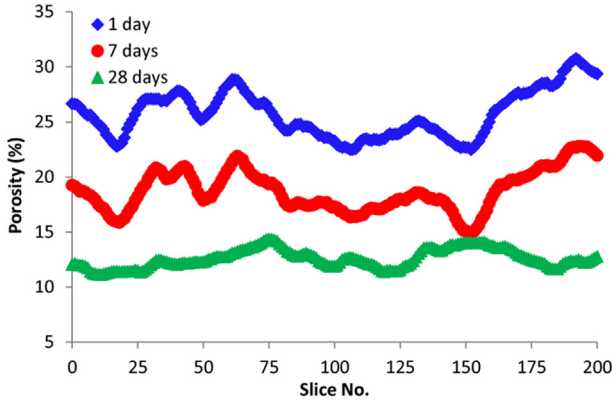**Fig. 2.** Different phases in cement paste at 7 days of curing: (a) capillary pores; (b) anhydrous cement grains.

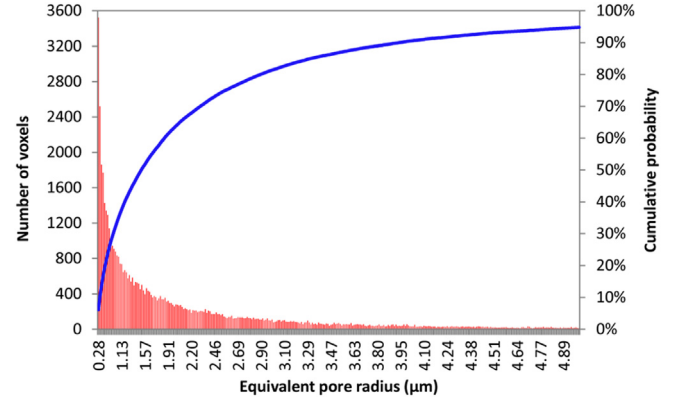**Fig. 3.** Porosity obtained for each 2D image of cement paste along *Z*-direction.
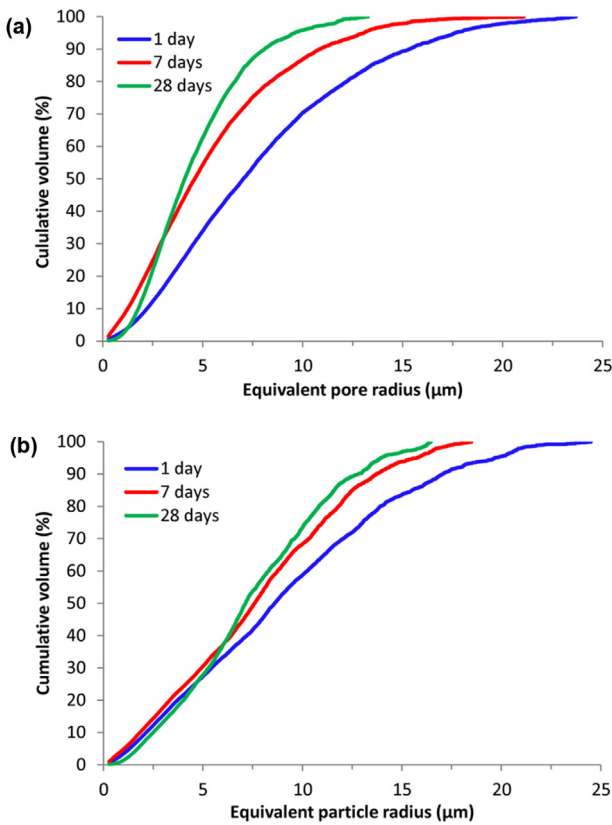

Fig. 4. Size distributions of pore and unhydrated cement particle of cement paste with various curing ages: (a) pore size distribution; (b) particle size distribution of unhydrated cement.

distributions of cement pastes with curing ages of 1, 7 and 28 days. It is obvious that both pore size and particle size of unhydrated cement are reduced with increasing curing age due to the progress of cement hydration. In addition, cement paste at 1 day contains more big pores and unhydrated cement particles compared to 7- and 28-day old cement pastes. In order to further illustrate the pore size distribution of cement paste, the histogram of pore size distribution of cement paste at 28 days of curing with cumulative probability distribution for pores with radii less than 5 μm is depicted in Fig. 5. It can be seen clearly that most of pores in the sample are small pores. Pores with radii less than 5 μm occupy 95% probability and the remaining 5% probability is left for pores with radii larger than 5 μm.

Fig. 5. Pore size distribution of cement paste at 28 days of curing.

3. Micromechanical modelling

Herein, a microstructure-informed site-bond model is proposed and developed for micromechanical modelling by incorporating the obtained experimental microstructural characteristics of cement paste into basic site-bond model for elasticity. The theoretical background of site-bond model, and modelling and simulation procedure are described in detail below.

3.1. Basic site-bond model

In the basic site-bond model, a material volume is represented by an assembly of truncated octahedral cells, each of which consists of six square and eight regular hexagonal faces, as shown Fig. 6a. The truncated octahedron is considered to be the better choice for a regular representation of the microstructure compared to other regular cell shape, such as cube, regular hexagonal prism and rhombic dodecahedron, the number of cell faces of which are 6, 8 and 12, respectively. The cell centre is regarded as a site linking to its neighbouring sites by fourteen bonds. These bonds are classified into two groups: B_1 includes six bonds in principal directions (normal to the square faces) and B_2 consists of eight bonds in octahedral direction (normal to the hexagonal faces) as illustrated in Fig. 6b. The bonds are modelled with a bundle of elastic-brittle normal and shear springs to represent the relative deformations between adjacent cells, as plotted in Fig. 6c. By assuming shear springs have identical stiffness coefficients, four spring constants can be derived as follows based on the equivalence of the strain energy density of the discrete cell to the continuum system [32]:

$$k_n^p = \frac{(3-4v)EL}{8(1+v)(1-2v)}; \quad k_n^o = \frac{(1+8v)EL}{8(1+v)(1-2v)}; \quad k_s^p = k_s^o$$
$$= \frac{(1-4v)EL}{8(1+v)(1-2v)} \tag{1}$$

where k_n^p and k_s^p denote the stiffness coefficients of normal and shear springs in principal direction, k_n^o and k_s^o represent the stiffness coefficients of normal and shear springs in octahedral direction, E and v are Young's modulus and Poisson's ratio of the material respectively, L is the spacing between two adjacent sites in principal directions.

The analytically derived spring stiffness coefficients were validated by benchmark simulations including uniaxial tension and plane-strain tension in previous work [32]. It was shown that the simulated overall mechanical constants, such as elastic modulus, Poisson's ratio and shear modulus are in good agreement with the theoretical values. In addition, the proposed lattice is able to
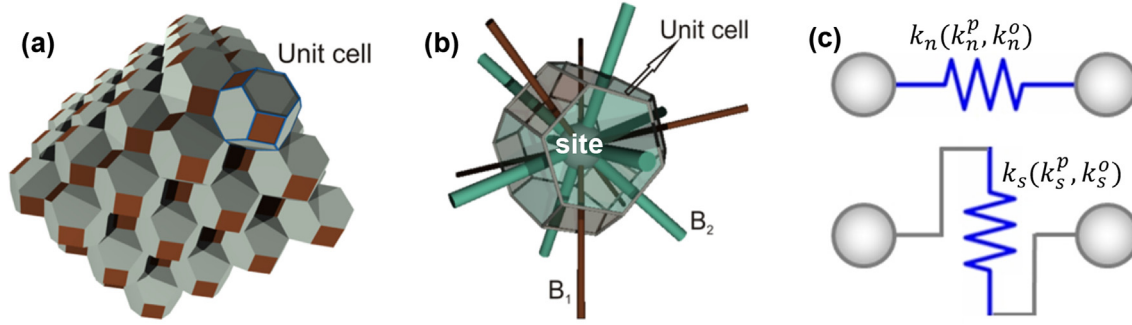
Fig. 6. Cellular lattice structure: (a) site-bond assembly; (b) unit cell with bonds; (c) normal and shear springs.

represent any isotropic elastic materials with Poisson's ratio in the range from −1 to 1/2, which covers all engineering materials.

3.2. Microstructure-informed site-bond model

The microstructure-informed site-bond model is constructed by incorporating the microstructural characteristics of cement paste into the basic site-bond model based on a random allocation of features, pores and anhydrous cement grains, with sizes belonging to the experimentally measured distributions. Firstly, anhydrous cement grains of different sizes are randomly distributed to all sites of the cellular structure according to the experimental particle size distribution plotted in Fig. 4. A generator of uniformly distributed random numbers $0 \leq r < 1$ is used to assign grains with different sizes to individual sites. For each site, a random number r is generated and the assigned grain size is $R_i = F^{-1}(r)$, where $F(R_i)$ is the cumulative probability of grain sizes shown in Fig 5. As a result, each cell has one spherical anhydrous cement grain with size R_i. Secondly, the cell size, L, is calculated from the volume fraction of anhydrous cement grains, ϕ_a, and the volume of the cellular structure with N cells via $\frac{\phi_a N L^3}{2} = \sum_i \frac{4\pi R_i^3}{3}$. Lastly, pores are assigned randomly to the bonds using the same method described above. The assignment continues until the prescribed porosity in the modelled material volume is reached. Fig. 7 illustrates a comparison of the simulated and experimental pore and anhydrous cement size distributions for cement paste at 28 days of curing. This indicates that the simulated size distributions of pore and unhydrated cement particles fit the measured size distributions obtained from X-ray micro-CT very well. The remaining volume represents
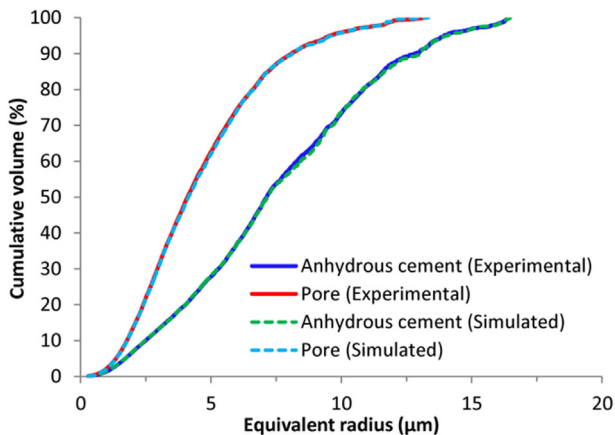

Fig. 7. Comparison of the simulated and experimental size distributions of pore and unhydrated cement particle of cement paste at 28 days of curing.

hydration product. Thus, the microstructure-informed site-bond model made up of pore, anhydrous cement grain and hydration product is established to incorporate the microstructure of cement paste into the basic site-bond model.

As introduced in Section 3.1, the stiffness coefficients of normal and shear springs in each bond are functions of macroscopic mechanical constants (Young's modulus E and Poisson's ratio v) of the represented homogeneous solid and cell size L. Since the microstructure-informed site-bond model has multiphase and porous features, it is necessary to homogenize the elastic properties of anhydrous cement grain and hydration product in the modelled cellular structure and to take into account pore effect. For this purpose, the effective Young's modulus E_{eff} and Poisson's ratio v_{eff} of a composite of anhydrous cement grain and hydration product, and effective cell size L_{eff} are defined and used instead of E, v, and L to calculate stiffness coefficients of springs according to Eq. (1).

Taking 28-day old cement paste for example, its porosity and volume fraction of anhydrous cement grains are 12.58% and 8.65%, respectively, as presented in Section 2. The remaining 78.77% is hydration product. For a composite of anhydrous cement grain and hydration product, anhydrous cement grain only occupies 9.9% of the volume. For this case, the Mori-Tanaka (M-T) method is appropriate for deriving effective elastic properties of the composite, since it has been shown to provide good estimates of the effective moduli of a two-phase composite, particularly when the volume fraction of the inclusion (herein, it is anhydrous cement grain) is low and the shape of the inclusion is spherical [10]. The M-T method is expressed by the following equations:

$$K_{eff} = K_h + \frac{\phi_a(K_a + K_h)(3K_h + 4G_h)}{3K_h + 4G_h + 3(1 - \phi_a)(K_a - K_h)} \quad (2)$$

$$G_{eff} = G_h + \frac{5\phi_a G_h(G_a - G_h)(3K_h + 4G_h)}{5G_h(3K_h + 4G_h) + 6(1 - \phi_a)(G_a - G_h)(K_h + 2G_h)} \quad (3)$$

$$E_{eff} = \frac{9K_{eff}G_{eff}}{3K_{eff} + G_{eff}}; \quad v_{eff} = \frac{3K_{eff} - 2G_{eff}}{2\left(3K_{eff} + G_{eff}\right)} \quad (4)$$

where K_{eff} and G_{eff} represent the effective bulk and shear moduli of the composite of anhydrous cement grain and hydration product, ϕ_a denotes the volume fraction of anhydrous cement of the composite, K_a, K_h, G_a and G_h are the bulk and shear moduli of anhydrous cement and hydration products, respectively.

The presence of a pore in a bond affects both the elastic constants and the failure propensity of the bond. The pore modifies the bond length to an effective value, L_{eff}, which can be calculated from the effective volume of the polyhedron between two neighbouring
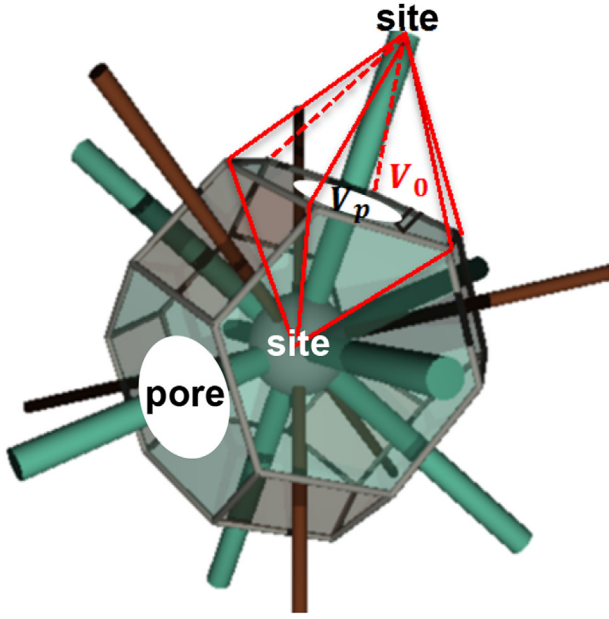
Fig. 8. Schematic illustration of microstructure-informed site-bond model with anhydrous cement grains at sites and pores on surfaces.

sites, V_{eff}, i.e. the volume of the polyhedron V_0 less the volume of the pore V_p, as shown in Fig. 8. Due to the different shape of polyhedrons in principal and octahedral directions, their volumes are different: $V_{p,0} = L^3/24$ for the polyhedron in principal direction, and $V_{0,0} = 3L^3/32$ for the polyhedron in octahedral direction. Thus, the corresponding effective cell sizes can be written as follows

$$L_{p,eff} = \sqrt[3]{24(V_{p,0} - V_p)}; \quad L_{o,eff} = \sqrt[3]{32(V_{0,0} - V_p)/3} \tag{5}$$

The spring constants of each bond, accounting for the pore associated with it, are calculated by substituting Eqs. (4) and (5) into Eq. (1) to replace E, ν and L with E_{eff}, ν_{eff} and L_{eff}.

3.3. Failure criterion

For microstructure-informed site-bond model, the spring elastic-brittle behaviour is represented by linear elastic and linear softening branches separated by a damage initiation point. The elasticity is dictated by Eq. (1) for given macroscopic elastic properties and microstructure-related length scale. The softening branch approximates the local post-initiation resistance of the matrix to failure. The area under the softening branch represents the additional energy required to separate two cells along their common interface, from the initiation of damage to final failure. The constitutive models for normal and shear springs are illustrated in Fig. 9, where $u_{t,max}$ and $u_{s,max}$ are the deformation of the normal and shear springs at damage initiation with corresponding maximum normal $F_{t,max}$ and shear forces $F_{s,max}$; $w_{t,max}$ and $w_{s,max}$ represent the deformation of the normal and shear springs at failure (set to $2u_{t,max}$ and $2u_{s,max}$, respectively); $K_n = F_{t,max}/U_{t,max}$ is the stiffness coefficient of the normal spring and $K_s = F_{s,max}/U_{s,max}$ is the stiffness coefficient of the shear spring. For normal springs, failure in compression is not allowed, which is achieved by setting the critical compressive deformation as $u_{c,max} = -10u_{t,max}$ and the maximum compressive force as $F_{c,max} = -10F_{t,max}$.

In this study, the energy-based failure criterion is applied. The shaded area in Fig. 9 represents the critical local failure energy, G_f, of a bond. This is calculated via $G_f = 2\gamma A_e$, where γ a prescribed surface energy (material parameter), and A_e is the effective face, i.e. the original face area A_0 less the cross-section area of the pores assigned to the face, A_p. Due to the existence of pores with different sizes on bonds (faces), the critical failure energies of bonds vary from the maximum failure energy $2\gamma A_0$ for bonds with no pores to zero for pore area close to the intact area of the face, e.g. square face or hexagonal face. If the pore area in a bond is equal to or larger than the corresponding face area, this bond is removed before loading.

3.4. Modelling and simulation

In this work, a material volume of size $20L \times 20L \times 20L$ is used. The corresponding cellular structure is made up of 17,261 cells; the site-bond model has the same number of sites and 113,260 bonds. The size of unit cell L can be determined based on the obtained microstructural information of cement paste from X-ray micro-CT following the procedure described in Section 3.2. As such, the experimental microstructure of cement paste is mapped to and represented by the microstructure-informed site-bond model. Table 1 shows the used elastic constants and surface energies of different phases in cement paste. Herein, it should be pointed out that the hydration product in Table 1 is considered as a composite of C–S–H and CH. The volume fractions of these two phases in hydration product would change with time. However, C–S–H and CH are difficult to be detected and identified with each other by using X-ray micro-CT due to the similarity in density. Therefore, the mechanical properties of hydration product are assumed constant for simplicity in this work. Uniaxial tension is considered. The loads
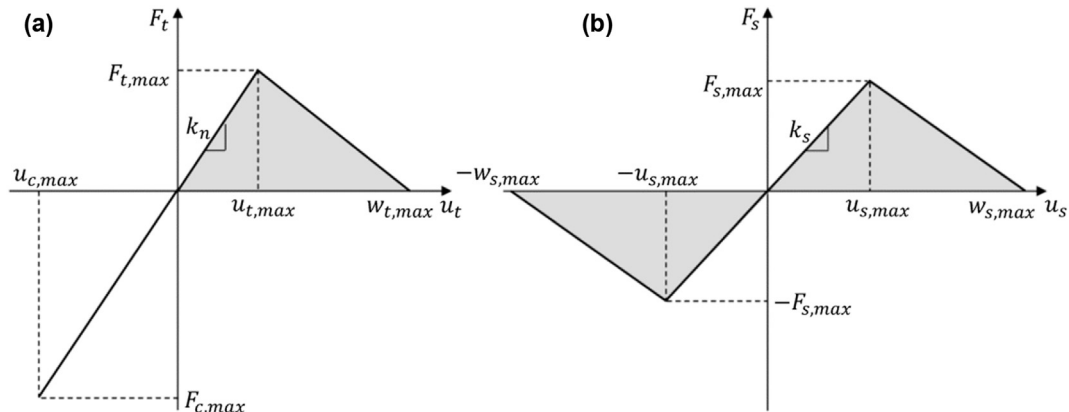

Fig. 9. Constitutive law and failure criteria for microstructure-informed site-bond model: (a) normal spring; (b) shear spring.

Table 1
Elastic constants and surface energy of different phases (Zhang and Jivkov, 2014).

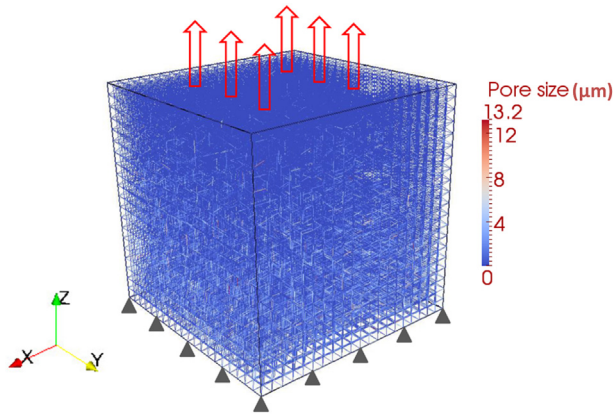| Phase	E (GPa)	v	K (GPa)	G (GPa)	$\gamma (mJ/m^2)$
Anhydrous cement grain	139.9	0.30	116.7	53.8	—
Hydration product	29.2	0.24	18.7	11.8	50
Pore	0	0	0	0	—

Fig. 10. Uniaxial tensile test on the microstructure-informed site-bond model for cement paste at 28 days of curing.

are applied via prescribed displacements to the boundary sites on top surface of the lattice system. The bottom surface is fixed and the other four surfaces are free. A schematic illustration of uniaxial tensile test on the microstructure-informed site-bond model for cement paste at 28 days of curing is given in Fig. 10. The bonds are presented in different colours (in web versaion) with dark red representing bonds with larger pores and blue denoting bonds with smaller pores. It can be seen that the spatial distribution of pore size is random. Most of larger pores are located around the centre between the top and bottom surfaces.

At each load step, the forces and deformations are obtained and the bond energies are calculated. The bond fails when its energy reaches the assigned critical failure energy, mimicking the creation of a micro-crack along the interface between the two cells joined by the bond. Upon failure the bond is removed from the site-bond assembly. The simulation is continued until the assembly is disintegrated or a prescribed strain is reached. Thus, the fracture

process can be obtained by the generation and evolution of micro-crack population under loading step by step.

4. Results and discussion

4.1. Elastic properties

Fig. 11 shows the simulated stress—strain response for cement pastes at 1, 7 and 28 days under uniaxial tension. It can be seen that the initial elastic part is perfectly linear, as represented by black dashed lines. Beyond the linear response, "graceful" quasi-brittle non-linearity prior to the peak stress is observed. The last point of the stress—strain curve corresponds to final failure. Compared to 7- and 28-day old cement pastes, cement paste with curing age of 1 day appears to be much more brittle, which can be attributed to the higher porosity and larger pore size at 1 day than those at 7 and 28 days, as shown in Figs. 3 and 4. Additionally, for 28-day old cement paste, an obvious softening branch can be found before the final failure.

From this curve, several important macroscopic parameters, such as elastic modulus, tensile strength, strain at failure point and fracture energy of cement paste, can be acquired. These parameters play crucial roles in the prediction of mechanical behaviours and fracture process of cement-based materials at meso-level, i.e. mortar and concrete (see e.g. Ref. [33]). The global elastic modulus corresponds to the slope of the stress—strain curve at the linear elastic stage. The tensile stress and strain at failure point are considered to be the tensile strength and peak strain, respectively.

Fig. 12 shows the time evolution of Young's modulus and tensile strength of cement paste. As expected, there is an increase in both Young's modulus and tensile strength with curing, which is a result of the continued cement hydration reaction and microstructure development of cement paste during curing. For the purpose of validation, the available experimental data taken from Refs. [4,5,11,16,34,35] are plotted together in Fig. 12. It should be mentioned that the w/c ratio of cement paste specimens in their experiments was 0.5, which is the same as that used in this work. It can be seen that the simulated Young's moduli show a good agreement with the experimental data, in particular for the cement paste specimens with curing age of 1 and 28 days. In addition, there exists an obvious variation of the measured Young's moduli of cement paste at 28 days by different researchers, which can be mainly attributed to the different types of cement used in their experiments. In Refs. [4,34], the used cement was ordinary Type I Portland cement, which is the same as that studied in the simulation. However, in Ref. [11] the used cement was ASTM D cement,
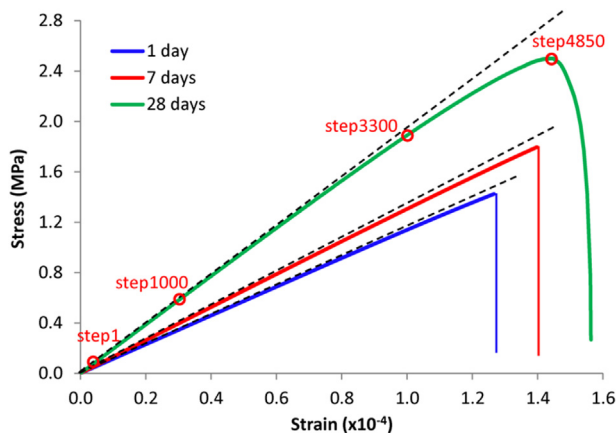

Fig. 11. Stress—strain response of cement pastes with various curing ages under uniaxial tension.
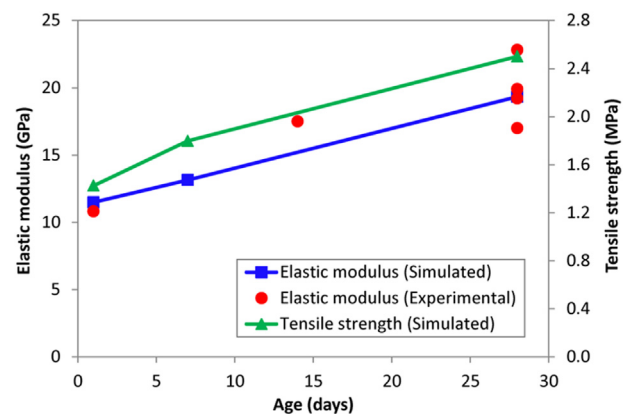

Fig. 12. Evolution of elastic modulus and tensile strength of hardened cement paste: experimental data taken from Refs. [4,5,11,16,34,35].

the chemical composition of which is somewhat different from that of Type I cement. As can be seen from Fig. 12, there is an obvious increase in tensile strength of cement paste with increasing curing age from 1 day to 7 days, followed by a gradual increase as curing age changes from 7 days to 28 days. Moreover, the strain at failure point increases with increasing curing age as a result of an obvious decrease in both porosity and pore size of hardened cement paste.

The fracture energy that is an essential input to continuum-based fracture models, e.g. cohesive zone model, can be calculated as the area under the stress–displacement curve that is converted from the stress–strain response shown in Fig. 11. It denotes all energy lost in distributed micro-cracking up to eventual rupture divided by the cross-section area of cement paste specimen. Further insight into this process can be obtained from the development of fracture process as described below.

4.2. Fracture processes

Fig. 13 shows the fracture processes in 28-day old cement paste under uniaxial tension (see Fig. 10) at loading steps of 1, 1000, 3300 and 4850 corresponding to stress–strain curve in Fig. 11. As can be seen from Fig. 13a, several micro-cracks initiate around the middle of the specimen after loading. These form by failure of bonds with large pores; compare with Fig. 10. Thus micro-crack initiation is triggered firstly by large pores in this region resulting in low critical

failure energies of these bonds. Bond failures progress with the load increase, Fig. 13b, but the micro-crack population remains relatively discrete: isolated failures, no observable localisation. Comparison with Fig. 11 suggests that isolated failures have a negligible contribution to the nonlinear stress–strain response. With further increase in loading, new micro-cracks are gradually generated, Fig. 13c and d. This is accompanied now by propagation and coalescence of existing micro-cracks forming clusters of free surfaces. The formation of larger free surfaces results in the clear non-linearity observable in Fig. 11. The peak in the stress–strain curve is reached via an avalanche-type failure, typical for tensile response, causing the separation of the whole structure into a collection of disjoint regions.

5. Conclusions

This work presents a micromechanical modelling of mechanical properties and fracture of hydrating cement paste based on proposed microstructure-informed site-bond method. The microstructure information of cement pastes at different curing ages obtained from high resolution X-ray micro-CT is incorporated into the site-bond assembly. The deformation and failure properties of the bonds are determined from microstructure-dictated length and energy parameters. The micro-crack evolution is simulated by
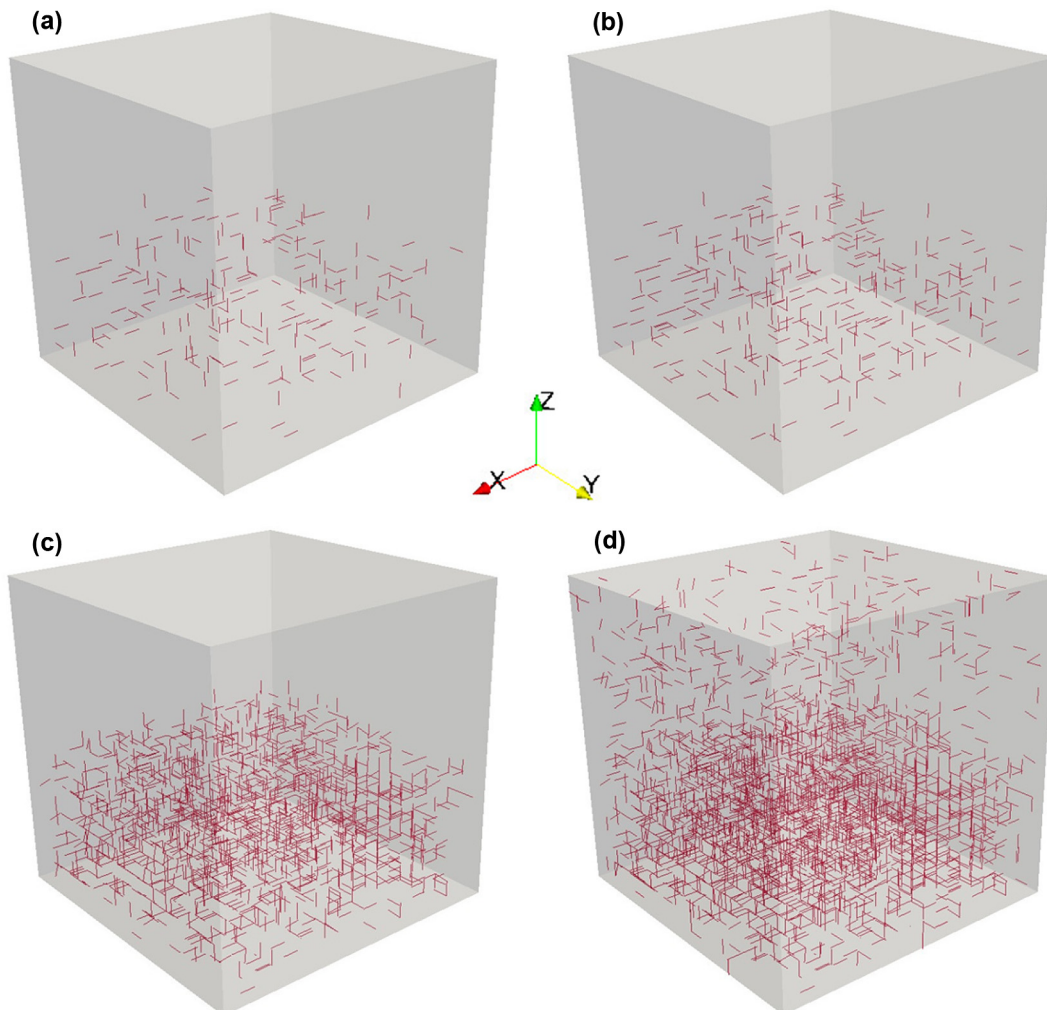

Fig. 13. Fracture process in 28-day old cement paste under uniaxial tension corresponding to the stress–strain curve in Fig. 11: (a) step1; (b) step1000; (c) step3300; (d) step4850.

removal of bonds. From the findings of the present study, the following conclusions can be drawn:

— Both porosity and pore size of cement paste decrease with increasing curing time. For cement paste with w/c ratio of 0.5, there is clear decrease in porosity from 25.69% to 12.58%, as age of cement paste increases from 1 day to 28 days. Meanwhile, particle size and volume fraction of anhydrous cement decrease as well.
— The microstructural evolution of cement paste due to cement hydration results in the development of mechanical properties (elastic modulus and tensile strength) of hardening cement paste.
— The simulated elastic properties of hydrating cement paste are in very good agreement with existing experimental data. Notably, the proposed site-bond models involve only data for sizes and interrelations of cement constituents without further empiricism.
— Micro-cracking initiates at pre-existing defects, e.g. large pores. As far as the micro-cracks remain isolated, i.e. in a discrete population, their effect on longer-scale behaviour is negligible and might be undetected by macroscopic experiment.
— Propagation and coalescence of micro-cracks, forming larger internal free surfaces, causes the observable non-linear response prior to peak load. The final specimen disintegration appears as avalanche-type failure at peak load.

The damage evolution under more complex loadings, e.g. triaxial and bending, is of larger practical relevance and will be the focus of future works, following the methodology presented in Ref. [28]. Additionally, the obtained fracture energy of cement paste in this work will be used as input for modelling of mechanical properties and fracture behaviour of cement mortar and concrete at meso-level based on a two-scale approach, which is a subject of ongoing work and will be presented in a future publication.

Acknowledgements

References

[1] Zhang M, Ye G, van Breugel K. Multiscale lattice Boltzmann-finite element modelling of chloride diffusivity in cementitious materials. Part I: algorithms and implementation. Mech Res Commun 2014;58:53–63.
[2] Ma HY, Li ZJ. Multi-aggregate approach for modeling interfacial transition zone in concrete. Aci Mater J 2014;111(2):189–99.
[3] Bernard O, Ulm FJ, Lemarchand E. A multiscale micromechanics-hydration model for the early-age elastic properties of cement-based materials. Cem Concr Res 2003;33(9):1293–309.
[4] Constantinides G, Ulm FJ. The effect of two types of C-S-H on the elasticity of cement-based materials: results from nanoindentation and micromechanical modeling. Cem Concr Res 2004;34(1):67–80.
[5] Sanahuja J, Dormieux L, Chanvillard G. Modelling elasticity of a hydrating cement paste. Cem Concr Res 2007;37(10):1427–39.
[6] Zheng JJ, Zhou XZ, Shao L, Jin XY. Simple three-step analytical scheme for prediction of elastic moduli of hardened cement paste. J Mater Civ Eng 2010;22(11):1191–4.
[7] Zhao XH, Chen WF. The effective elastic moduli of concrete and composite materials. Compos Part B-Eng 1998;29(1):31–40.
[8] Pichler B, Hellmich C. Upscaling quasi-brittle strength of cement paste and mortar: a multi-scale engineering mechanics model. Cem Concr Res 2011;41(5):467–76.
[9] Pichler C, Metzler G, Niederegger C, Lackner R. Thermo-mechanical optimization of porous building materials based on micromechanical concepts: application to load-carrying insulation materials. Compos Part B Eng 2012;43(3):1015–23.
[10] Mori T, Tanaka K. Average stress in matrix and average elastic energy of materials with misfitting inclusions. Acta Metall Mater 1973;21(5):571–4.
[11] Haecker C, Garboczi EJ, Bullard JW, Bohn RB, Sun Z, Shah SP, et al. Modeling the linear elastic properties of Portland cement paste. Cem Concr Res 2005;35(10):1948–60.
[12] Bentz DP. Three-dimensional computer simulation of portland cement hydration and microstructure development. J Am Ceram Soc 1997;80(1):3–21.
[13] Smilauer V, Bittnar Z. Microstructure-based micromechanical prediction of elastic properties in hydrating cement paste. Cem Concr Res 2006;36(9):1708–18.
[14] Valentini L, Parisatto M, Russo V, Ferrari G, Bullard JW, Angel RJ, et al. Simulation of the hydration kinetics and elastic moduli of cement mortars by microstructural modelling. Cem Concr Comp 2014;52:54–63.
[15] Bernard F, Kamali-Bernard S. Predicting the evolution of mechanical and diffusivity properties of cement pastes and mortars for various hydration degrees – a numerical simulation investigation. Comp Mater Sci 2012;61:106–15.
[16] Stefan L, Benboudjema F, Torrenti JM, Bissonnette B. Prediction of elastic properties of cement pastes at early ages. Comp Mater Sci 2010;47(3):775–84.
[17] Hain M, Wriggers P. Numerical homogenization of hardened cement paste. Comput Mech 2008;42(2):197–212.
[18] Huang J, Krabbenhoft K, Lyarnin AV. Statistical homogenization of elastic properties of cement paste based on X-ray microtomography images. Int J Solids Struct 2013;50(5):699–709.
[19] Jivkov AP, Engelberg DL, Stein R, Petkovski M. Pore space and brittle damage evolution in concrete. Eng Fract Mech 2013;110:378–95.
[20] Qian Z, Schlangen E, Ye G, van Breugel K. Prediction of mechanical properties of cement paste at microscale. Mater Construc 2010;60(297):7–18.
[21] Schlangen E, van Mier JGM. Experimental and numerical analysis of micro-mechanisms of fracture of cement-based composites. Cem Concr Comp 1992;14:105–18.
[22] van Breugel K. Numerical-simulation of hydration and microstructural development in hardening cement-based materials .1. Theory. Cem Concr Res 1995;25(2):319–31.
[23] van Breugel K. Numerical-simulation of hydration and microstructural development in hardening cement-based materials .2. Applications. Cem Concr Res 1995;25(3):522–30.
[24] Ye G, van Breugel K, Fraaij ALA. Three-dimensional microstructure analysis of numerically simulated cementitious materials. Cem Concr Res 2003;33(2):215–22.
[25] Zhang M, Ye G, van Breugel K. Microstructure-based modeling of water diffusivity in cement paste. Constr Build Mater 2011;25(4):2046–52.
[26] Bernard F, Kamali-Bemard S, Prince W. 3D multi-scale modelling of mechanical behaviour of sound and leached mortar. Cem Concr Res 2008;38(4):449–58.
[27] Jivkov AP, Yates JR. Elastic behaviour of a regular lattice for meso-scale modelling of solids. Int J Solids Struct 2012;49(22):3089–99.
[28] Jivkov AP. Structure of micro-crack population and damage evolution in quasi-brittle media. Theor Appl Fract Mec 2014;70:1–9.
[29] Zhang M, Jivkov AP. Microstructure-informed modelling of damage evolution in cement paste. Constr Build Mater 2014;66:731–42.
[30] Zhang M, He Y, Ye G, Lange DA, van Breugel K. Computational investigation on mass diffusivity in Portland cement paste based on X-ray computed micro-tomography (mu CT) image. Constr Build Mater 2012;27(1):472–81.
[31] Ma HY, Li ZJ. Realistic pore structure of Portland cement paste: experimental study and numerical simulation. Comput Concr 2013;11(4):317–36.
[32] Zhang M, Morrison CN, Jivkov AP. Meso-scale site-bond model for elasticity: theory and calibration. Mater Res Innov 2014;18:982–6.
[33] Chaudhuri P. Multi-scale modeling of fracture in concrete composites. Compos Part B Eng 2013;47:162–72.
[34] Sun Z, Ye G, Shah SP. Microstructure and early-age properties of portland cement paste - effects of connectivity of solid phases. Aci Mater J 2005;102(2):122–9.
[35] Boumiz A, Vernet C, Tenoudji FC. Mechanical properties of cement pastes and mortars at early ages – evolution with time and degree of hydration. Adv Cem Based Mater 1996;3(3–4):94–106.